PHOTONICS Research

Discretization of annular-ring diffraction pattern for large-scale photonics beamforming

Aroutin Khachaturian,* Reza Fatemi, Artsroun Darbinian, and Ali Hajimiri

California Institute of Technology, Pasadena, California 91125, USA
Corresponding author: akhachat@caltech.edu

A solid-state active beamformer based on the annular-ring diffraction pattern is demonstrated in an integrated photonic platform. Such a circularly symmetric annular-ring aperture achieves a radiating element limited field of view. Furthermore, it is demonstrated that a multi-annular-ring aperture with a fixed linear density of elements maintains the beam efficiency for larger apertures while reducing the beamwidth and side-lobe level. A 255-element multi-annular-ring optical phased array with active beamforming is implemented in a standard photonics process. A total of 510 phase and amplitude modulators enable beamforming and beam steering using this aperture. A row–column drive methodology reduces the required electrical drivers by more than a factor of 5.   © 2022 Chinese Laser Press

1. INTRODUCTION

Integrated solid-state photonic beamformers (optical phased arrays, or OPAs) have the potential to reduce the cost, size, and implementation complexity of many photonic systems compared to their bulk optics and micro-electromechanical systems (MEMS) counterparts [1,2]. These solid-state beamformers have been recently demonstrated for lidar [3,4], photonic beam steering [5–7], medical imaging [8], and remote sensing [9] applications. In particular, standard silicon photonics processes can further reduce the cost and increase the yield and reliability of such systems [6,10–12]. However, there are several challenges associated with the realization of large-scale, solid-state beamformers.

Most integrated photonic dielectric waveguides and radiators have a minimum size and spacing on the order of the wavelength. Any 2D aperture constructed with uniformly spaced radiators will require a large inter-element spacing to route the signals to the inner elements of the array. This leads to minimum pitch and spacing constraints that then lead to a reduced field of view (FOV) and increased grating lobes as the size of the array aperture increases. There are two categories of architectures that have been used to overcome this problem. One class of architectures uses a wavelength-sensitive 1D grid array of radiating elements to steer the beam in one direction and sweep the wavelength of the laser to steer the beam in the perpendicular direction [10,11,13–15]. This method removes the planar routing restriction at the cost of an increased laser source and system complexity. Typically, a broadly tunable laser source (around 100 nm of wavelength tunability) is required to

achieve a moderate FOV (around 20°) [10,14,16]. Such tunable lasers are more complex and hence more costly compared to their single wavelength counterparts. Furthermore, such OPAs cannot offer wavefront control in the steering direction controlled by the wavelength.

Another class of architectures uses sparse array synthesis techniques to construct a 2D grid array of radiating elements that permit routing the signals of the inner elements of the array [6]. Compared to their equal-sized aperture, half-wavelength spacing counterparts, sparse arrays reduce the number of the radiating elements and phase shifters required, thus reducing array control complexity, power consumption, heat dissipation, and system cost. Furthermore, such arrays can operate with a fixed-wavelength laser source. These 2D grid OPAs have advantages over their 1D grid aperture counterparts since they can offer full wavefront control with a fixed wavelength laser. However, sparse placement of the elements reduces the array gain and beam efficiency, which is also known as the "sparse array curse." This fact fundamentally limits the performance of sparse arrays for power transfer applications, making them more suitable for point-by-point imaging and sparse target detection applications. Furthermore, most sparse array synthesis techniques achieve target beam performance by the randomized placement of elements in a 2D grid given the constraints on the number of elements and planar signal routing. For example, genetic algorithms have been used for sparse array synthesis [6,17,18]. This optimization process is computationally expensive for larger aperture sizes with an increased number of elements and there is no guarantee of arriving at the optimal design.

One method to reduce the complexity of finding optimum sparse apertures is to take advantage of the basic properties of circularly symmetric apertures. The ideal symmetric aperture is circular, as shown in Fig. 1(a). The beam pattern of such an aperture can be computed by taking the Fourier transform of a circle:

$$|P_{circ}(\theta)| = |\mathcal{F}[circ(D)]| = \frac{J_1\left(\frac{kD}{2}\sin\theta\right)}{\frac{kD}{2}\sin\theta}, \qquad (1)$$

where P is the radiation pattern, θ is the elevation angle, D is the diameter of the circle, k is the wave number, and J_1 is the first-order Bessel function of the first kind. The beam intensity cross-section of such an aperture is shown in Fig. 1(d), as is described by the function $J(x)/x$. Another circularly symmetric aperture is the annular-ring aperture, which is shown in Fig. 1(b), and can be modeled by blocking the center region of a circular aperture. The far-field beam pattern for such an aperture is given by the Fourier transform of the difference of two circular apertures of diameters D and $D - \delta$:

$$|P_{Ring}(\theta)| = |\mathcal{F}[circ(D) - circ(D - \delta)]| = J_0\left(\frac{kD}{2}\sin\theta\right), \qquad (2)$$

where δ is small and J_0 is the zeroth-order Bessel function of the first kind. The beam intensity of this cross-section is shown in Fig. 1(d).

These beam patterns show that annular-ring apertures reduce the beamwidth at the cost of an increased side-lobe level (SLL) compared to their circular counterparts that have an aperture with a significantly larger area. More importantly, annular-ring apertures do not produce grating lobes. This annular-ring aperture can be realized in a planar photonics process. We can physically implement an OPA capable of active beam steering by placing radiating elements on this annular ring at half-wavelength spacing, as shown in Fig. 1(c). This discretized annular-ring array pattern approximates to the pattern

of a continuous annular-ring aperture, which is shown in Fig. 1(d), for a sufficiently large number of elements. It is possible to combine multiple such discretized annular rings to improve the OPA beamwidth and SLL, as shown in Fig. 1(e). In phased array theory, such multi-annular-ring apertures can be categorized under circular-aperture arrays [19–24]. The theoretical performance of uniform and nonuniform circular arrays and their application to an integrated OPA have been previously analyzed and discussed in Refs. [21,25]. Such symmetric apertures are advantageous over their rectangular counterparts since they exhibit minimal disturbance to the beamwidth and SLL when scanned azimuthally over the entire plane [26].

In this paper, we demonstrate what we believe, to the best of our knowledge, is the first implementation of such multi-annular-ring OPAs in a silicon photonics process and analyze the architectural advantages and the limitations of such OPAs. In the next section, we analyze the beamforming characteristics of such annular rings in the context of planar photonics platforms. Afterward, we present a 255-element silicon photonics implementation of such an annular-ring OPA transmitter with full amplitude and phase control for individual radiators. This OPA design can be modified to operate as a transceiver [27] or as a heterodyne receiver by incorporating balanced detectors [6]. We simplify the electrical drive interconnect complexity of such an OPA by using a row–column drive that reduces the total number of electrical interconnects from 510 nodes to 100 nodes. Finally, we discuss the beamforming optimization methodology of this large-scale OPA and demonstrate the beamforming and beam-steering capability of this OPA.

2. ANALYSIS OF ANNULAR-RING APERTURES

The discretized multi-annular-ring aperture can be generalized by creating M concentric rings, each with N_m isotropic radiators equidistant in arc length, where $m \in 1, 2, \ldots, M$, as shown in Fig. 1(e). Using the expression for the far-field radiation pattern or an array factor of a single annular-ring aperture
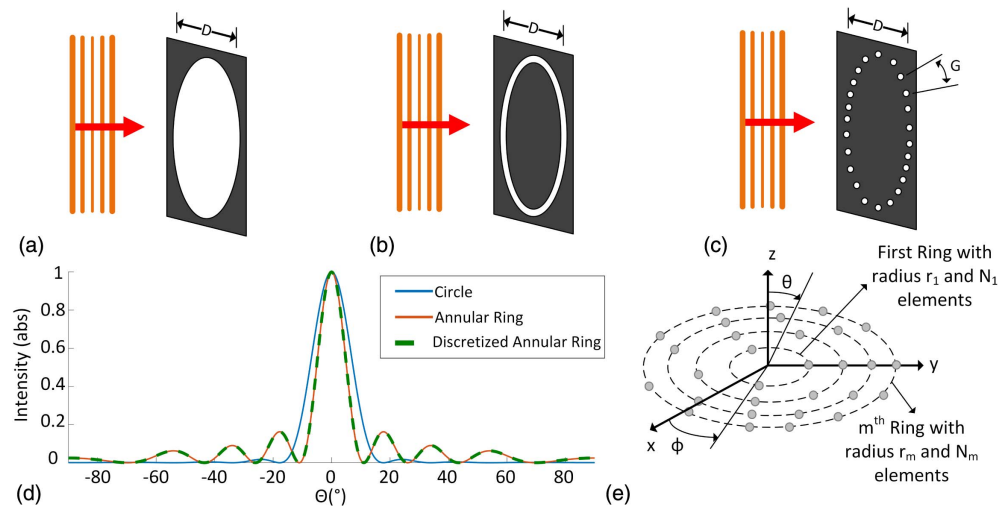
Fig. 1. Diffraction pattern of circularly symmetric apertures with diameter $D = 2\lambda$ when illuminated by a plane wave. (a) Circular aperture. (b) Annular-ring aperture. (c) Discretization of the annular ring with 25 points. $G \approx \lambda/2$ is the arc-length distance between two elements. (d) Diffraction pattern cross-section of apertures in (a), (b), and (c). (e) Generalization of discretized multi-annular-ring apertures equivalent to circular-grid phased arrays.

from Ref. [19], we can write the generalized array factor for a multi-annular-ring aperture as

$$|P(\theta,\phi,\theta_0,\phi_0)|$$

$$= \sum_{m=1}^{M}\sum_{n=1}^{N_m} I_{m,n}e^{jkr_m[\sin(\theta)\cos(\phi-\phi_{m,n})-\sin(\theta_0)\cos(\phi_0-\phi_{m,n})]}, \quad \textbf{(3)}$$

where $I_{m,n}$ is the E-field intensity for the particular element, r_m is the radius of the mth ring, $\phi_{m,n}=2\pi n/N_m$ is the angular position of the nth element in the aperture, and (θ_0,ϕ_0) pair describes the direction of the main beam. While amplitude apodization will help with SLL reduction, we limit this analysis to uniform excitation, $I_{m,n}=1$, in the broadside direction, $(\theta_0,\phi_0)=(0,0)$, unless otherwise stated.

A. Approximation of Continuous Annular-Ring Aperture

Using Eq. (3), we can compute the diffraction pattern of the continuous annular-ring aperture in Fig. 1(b) by assuming $M=1$ and replacing the summation of the discrete points by integration over the entire circumference:

$$|P(\theta)| = \int_{0}^{2\pi} e^{jkr\sin\theta\cos\phi_n}\mathrm{d}\phi_n = 2\pi J_0(kr\sin\theta). \quad \textbf{(4)}$$

After normalizing Eq. (4), the beam pattern is a Bessel function of order zero, which is identical to the diffraction pattern calculation for an annular ring in Eq. (2).

As shown in Fig. 1(d), placing discretized elements at distances up to half-wavelength spacing is equivalent to the continuous case with a Bessel function beam pattern for the entire FOV. As a result, the beam pattern of this circularly symmetric structure is independent of ϕ, which is desired for most beamforming applications. This simplified Bessel form can

be used as a first-order approximation to analyze sufficiently dense annular-ring arrays. If the distance (over the arc) between the radiating elements increases to larger values, the integration in Eq. (4) that leads to the Bessel function approximation no longer holds for the entire FOV. This is depicted in Fig. 2(a). Here, an annular-ring aperture with a 20 μm diameter and 1.55 μm wavelength is plotted for continuous/half-wavelength case (81 elements), 40, and 20 radiating elements. For the case of 40 radiating elements (1.6 μm arc length spacing), the Bessel approximation is valid up to 58°. For the case of 20 radiating elements (3.1 μm arc length spacing), the Bessel approximation is valid for θ up to 23°. The range of angles for which the Bessel form holds is approximately inversely proportional to the sparsity factor [annular-ring element density of $\rho_r = 2\lambda$ will result in the Bessel approximation being valid up to $90° \times (\lambda/2)/\rho_r = 22.5°$]. Furthermore, as the density of the elements along the arc (ρ_r) decreases, the SLL increases further. This makes the Bessel approximation inaccurate for sufficiently sparse annular-ring apertures. Therefore, for the remainder of this paper, the analysis of sparse annular-ring arrays (larger than the half-wavelength spacing of radiators on the arc length) is done using Eq. (3).

B. Annular-Ring Apertures with a Fixed Linear Density

This multi-annular-ring aperture given by Eq. (3) is circularly symmetric, and as a result, the placement of the radiating elements can be optimized for desired performance parameters with reduced computational complexity compared to their rectangular grid sparse apertures counterpart. Such multi-annular-ring apertures can be analyzed for any of the beamforming parameters such as beamwidth, SLL, beam efficiency (defined as the ratio of the optical power in the 3 dB
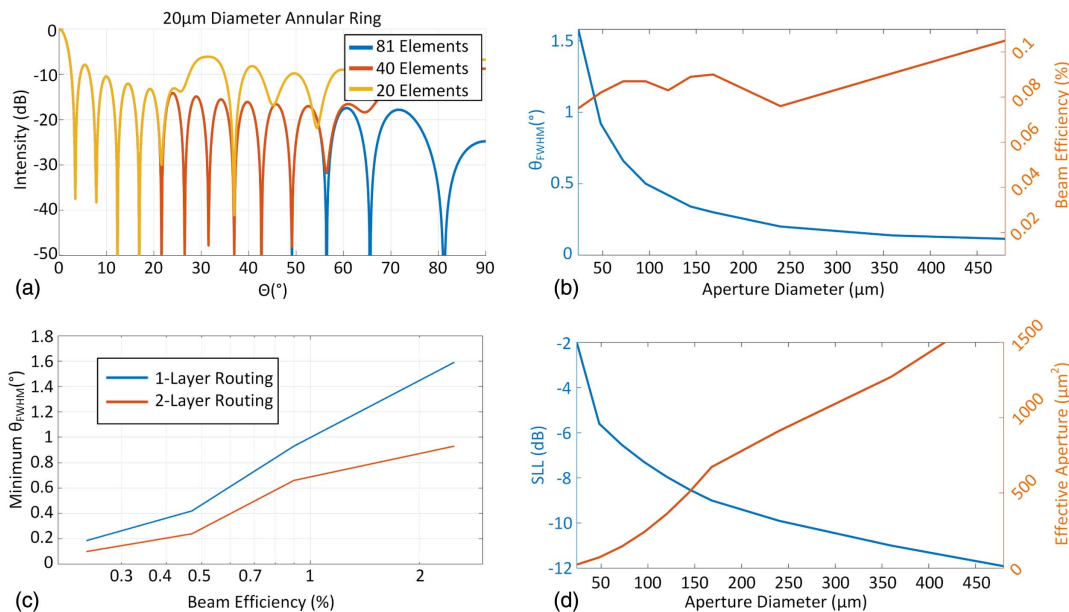
Fig. 2. (a) Effect of annular-ring discretization on the far-field array factor. A 20 μm diameter ring is plotted for a continuous annular-ring-slit aperture (or half wavelength-spacing elements), discretized with 40 isotropic radiators and 20 isotropic radiators. (b) Beamwidth and 3 dB beam efficiency trends as a function of phased array aperture diameter. (c) Minimum beamwidth as a function of 3 dB beam efficiency for linear density multi-annular-ring OPAs at the planar routing limits for single-layer and two-layer photonics process. (d) SLL and effective aperture as a function of aperture diameter.

beamwidth of the main lobe and the total power delivered to the aperture), and element count. In this work, we limit our analysis of annular-ring apertures to apertures with fixed linear density. In other words, we assume a constant elements per arc length density ($N_m = mN_1$) and linearly increase the ring radii ($r_m = mr_1$).

For such apertures with linear density, the planar photonic process parameters set the elements per arc length density as well as the minimum aperture diameter limits. For silicon photonics processes, the waveguides are typically 500 nm wide with a minimum pitch of 1 µm to reduce the electromagnetic coupling between the adjacent waveguides. Radiating elements can also be constructed at the size of the waveguides (500 nm). For a fixed linear density, the design values r_1 and N_1 set the beam efficiency of the aperture. Assuming $r_1 = 40$ µm and $N_1 = 20$, we can plot the beamwidth, beam efficiency, SLL, and effective aperture (total area of radiating elements) for different aperture sizes (values of M). Figure 2(b) shows that while the half beamwidth decreases for larger and larger apertures, the beam efficiency remains relatively constant. Since this aperture maintains a fixed linear density, the array sparsity factor remains the same, which explains the relatively constant value of the main beam efficiency. In other words, maintaining the linear density of the array ensures that as the array size increases the power in the main beam remains constant relative to the remaining power distributed among the side lobes. Furthermore, increasing the array size results in the remaining power distributing more evenly among the side lobes, reducing the peak SLL. This is shown in Fig. 2(d), where the SLL decreases as the aperture size gets larger and the effective aperture size also increases. Thus, multi-annular-ring apertures are good candidates for sparse phased-array receiver applications where the collection area and SLL are important performance metrics. Moreover, these plots suggest that for a given fixed linear density (r_1, N_1) pair the beam performance improves while the beam efficiency remains constant until the planar routing limitations limit the size of the aperture for the particular linear density. This provides a design methodology for multi-annular-ring apertures. We can proceed and calculate the largest apertures that can be constructed using these linear density annular-ring apertures. Assuming the waveguide and radiator size and pitch limitations of silicon photonics platforms mentioned above and using the symmetric nature of these apertures, multi-ring annular-ring apertures can be constructed starting from the innermost ring. Note that the waveguide minimum bend radius limitations are ignored in this analysis. The signal from the inner rings of the aperture is radially routed outside the aperture in all directions between the radiators on the outermost ring. The maximum aperture size is reached when the total inter-element spacing of the radiators in the outermost ring equals the total width and spacing required to route the signals to the radiators inside the aperture. We can plot the minimum achievable beamwidth, given the maximum aperture size, for a given beam efficiency for single-layer and two-layer photonic platforms, as shown in Fig. 2(c). Thus, a multi-annular-ring OPA implemented in a single-layer photonic platform with 0.9% beam efficiency (0.93° array beamwidth) and 90° 3 dB-beamwidth radiators can resolve. The beam

efficiency is defined as the ratio of the optical power in the 3 dB beamwidth of the main lobe and the total power delivered to the aperture. A two-layer photonic platform that is realized with a multilayer photonic process such as in Ref. [28] can double the number of signals routed for a given aperture size. Alternatively, a two-layer photonic process, in which the radiators are placed on the same photonic layer, allows the physical realization of a larger aperture with the same linear density and beam efficiency, which approximately doubles the number of resolvable points to 18,595 in the far field.

Figure 2(c) demonstrates the general trade-off between beam efficiency and minimum beamwidth, which is limited by the "sparse array curse." Nevertheless, the aperture efficiency can be moderately improved by using various array-synthesis techniques such as fine-tuning the position of the radiating elements inside the aperture or incorporating amplitude apodization. For example, a multi-annular-ring array with (r_1, N_1, M) = (10 µm, 20, 3) and 90° FOV radiators with uniform amplitude excitation results in a 0.66° beamwidth with 1.76% main beam efficiency. Introducing amplitude apodization [exciting the radiators in the first, second, and third annular rings with relative intensities of (1, 0.8, 0.6)] will slightly improve the main beam efficiency to 1.91% while increasing the beamwidth to 0.70°. A complete survey of various array-synthesis techniques to improve the performance of multi-annular-ring arrays is beyond the scope of this paper.

3. MULTI-ANNULAR-RING OPA IMPLEMENTATION

To demonstrate the beamforming and beam-steering capability of multi-annular-ring aperture OPAs, we implemented a five-annular-ring aperture OPA system with active beamforming in Advanced Micro Foundry's (AMF) standard photonics process. The die photo of this system is shown in Fig. 3. This OPA has a 400 µm diameter annular-ring aperture with 255 radiating elements with complete phase and amplitude control. The thermo-optic phase and amplitude modulators are distributed into four blocks and electrically connected in a row–column fashion to reduce the electrical interconnect density from order N^2 to order N. Amplitude modulation is achieved via a $1{:}2^N$ tunable amplitude distribution network that can be calibrated with only $N + 1$ integrated sniffer photodiodes. The design details of these three sub-blocks are examined in the following subsections.

A. Implemented Aperture

This multi-annular-ring OPA array factor was optimized based on a 1 µm minimum pitch in the waveguide routing with 2 µm × 5 µm compact photonics radiators, as shown in Fig. 4(c). Based on the analysis in Section 2.B, we incorporated a five-annular-ring ($M = 5$) aperture with a linear density ($r_1 = 40$ µm and $N_1 = 17$). As a result, 17, 34, 51, 68, and 85 radiators are placed on rings with radii, respectively, of 40 µm, 80 µm, 120 µm, 160 µm, and 200 µm, as shown in Fig. 4(a). This multi-annular-ring aperture maintains the Bessel form for a 2° FOV with a 0.2° theoretical beamwidth with no grating lobes in the full FOV. The cross-section of the radiation pattern for this OPA is shown in Fig. 4(b).
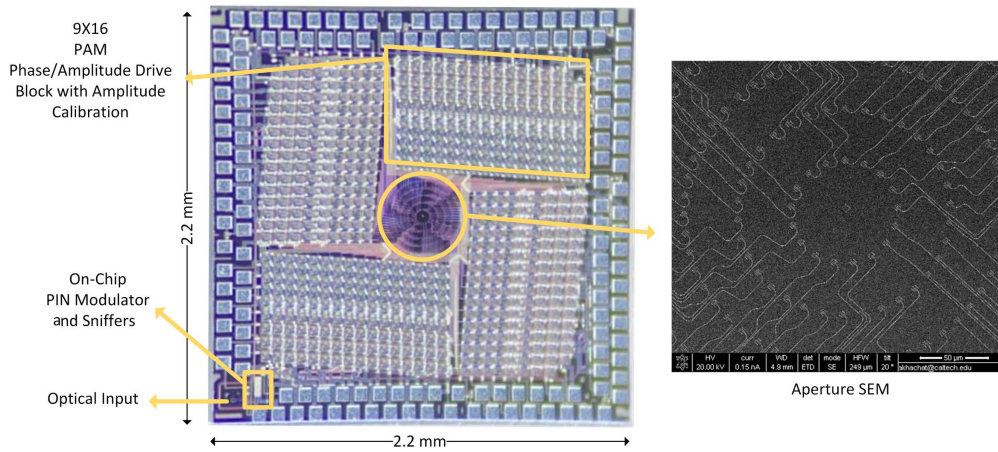
Fig. 3. Multi-annular-ring aperture OPA system. Die photo of the proposed design and SEM photo of the aperture. Phase and amplitude modulators are grouped into four blocks for symmetric layout.

The radiating element used in this aperture has a 3 dB far-field beamwidth of 23° × 16.3° with a more than 50% peak radiation efficiency at the optimum angle of 7.4° [29]. Furthermore, the 1 dB spectral bandwidth of the radiator is more than 400 nm, which makes these radiators insensitive to temperature and wavelength variations. As a result, the FOV of this aperture is limited by the FOV of the radiating element with a maximum SLL of –15.6 dB, as shown in Fig. 4(b). Furthermore, the theoretical resolution of this OPA is $115 \times 81 = 9315$ total points. The beam efficiency of this aperture is 0.15%. This is lower than the 44% beam efficiency of a uniform half-wavelength spacing array. This reduction in the main beam power efficiency compared to the

uniform half-wavelength spacing array is a measure of the sparsity of the aperture. In addition, the theoretical directivity for the multi-annular-ring array (assuming isotropic radiators) and the directivity of the individual radiators are 24 dB and 11 dB, respectively. Based on the 3 dB loss of the radiator, approximately 3 dB combined loss of the splitters and waveguides, and 35 dB directivity for the aperture, we estimate 39 dBm EIRP (effective isotropic radiated power) for 10 dBm input power into the array.

B. Row–Column Drive

The amplitude and phase modulators for the 255-element array are divided into four blocks. Both amplitude and phase
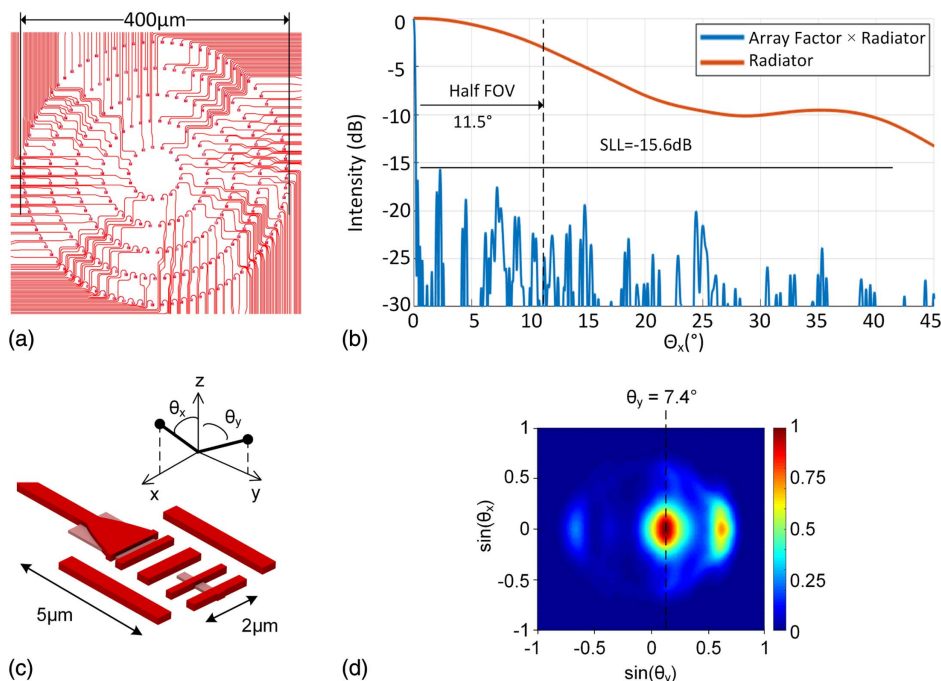
Fig. 4. (a) Layout and signal distribution for a 255-element annular-ring aperture. (b) Full AF of the aperture for $\phi = 0$, including the radiator's beam pattern. (c) Custom radiating element used in this OPA. (d) The far-field radiation pattern of the radiating element.

modulators incorporate a compact spiral thermo-optic phase shifter design to reduce the device footprint and increase isolation between radiating elements [29], as shown in Figs. 5(b) and 5(c). The amplitude modulation is achieved by a cascade of tunable optical couplers that split the light into 64 branches. This tunable power splitter requires 63 tunable couplers. The output of each tunable coupler passes through phase shifters before reaching the radiating elements to adjust the relative phase between elements. These 127 active components are electrically connected in a row–column fashion, as shown in Fig. 5(a). The tunable couplers are arranged in a 16×4 grid. There are 64 phase shifters in each block. In addition, there are 16 distributed dummy thermal phase shifters placed among the phase shifters to reduce the thermal gradient in the substrate. These phase shifters and dummy heaters are arranged in a 16×5 grid. These phase and amplitude modulator grids are connected as one unit in a 16×9 matrix resulting in $4 \times (16 + 9) = 100$ drive nodes for the full OPA. Four out of 16 rows of this 16×9 row-column drive matrix are shown in Fig. 5(a).

To achieve independent control of all phase and amplitude modulators, each of these four blocks is programmed by a time-domain demultiplexing technique that uses the thermal memory of these phase shifters. In this scheme, the modulators are programmed in continuous cycles. Each programming cycle, T, is divided into 16 time slots. During each time slot $(T/16)$, only one row of the phase shifter matrix is programmed using nine pulse-amplitude modulation (PAM) drivers that deliver the desired thermal power to elements in the active row and keep the remaining rows of the modulators in the off state. Each of the nine PAM drivers switches between 16 different values for each programming cycle, which allows 144 different values to be independently programmed in the 16×9 matrix. This is achieved by including a series diode with a resistive heater to prevent the flow of current through the turned-off columns of the array by keeping the diode in reverse bias. The series diode has a footprint of 200 μm^2 and adds 10% to the total area of the phase or amplitude modulator. Since these thermal phase shifters have a bandwidth on the order

of several kHz, having a programming period T in the MHz range ensures that all phase shifters maintain their temperature or programmed phase value. This row–column drive methodology reduces the required number of electrical interconnect nodes for an $N \times M = 16 \times 9$ array from 144 nodes to $N + M = 25$ nodes.

This row–column drive methodology trades the number of required drivers and system complexity with an increased requirement on driver bandwidth, output voltage swing, and drive signal complexity. Scaling the total number of phase and amplitude modulators by a factor of N^2 (doubling both rows and columns) increases the bandwidth requirement by a factor of N and increases the drive voltage requirement by a factor of $\sqrt{N}$. For example, if a PAM drive with 2 MHz bandwidth and 10 V output voltage swing is sufficient for a 16×9 array, increasing the number of phase and amplitude modulators by a factor of $N = 100$ to 14,400 increases the PAM bandwidth requirement to 20 MHz, which is available in modern electronic processes. Furthermore, the drive voltage requirement increases by a factor of $\sqrt{10}$ to 31 V, which can be realized using stacked-transistor driver topologies [29].

C. Amplitude Modulation with Simplified On-Chip Calibration

Amplitude modulation for the 255 elements in this design is achieved by cascading 8 one to two tunable optical couplers [Fig. 6(a)]. This design is advantageous over the conventional approach of dedicating one amplitude attenuator per signal path [27] because, for different amplitude configurations, the power is redistributed between different paths, and the total power delivered to the aperture remains constant. This distribution method can be used to deliver equal power to all elements or to achieve amplitude apodization for reduced SLL. Each output of these amplitude modulators has a 1% power splitter and a compact sniffer photodetector for on-chip calibration. The output of these photodiodes can be used to perform a one-time calibration to correct for fabrication mismatches in the tunable amplitude coupler and determine the drive voltage requirement for the amplitude modulators.
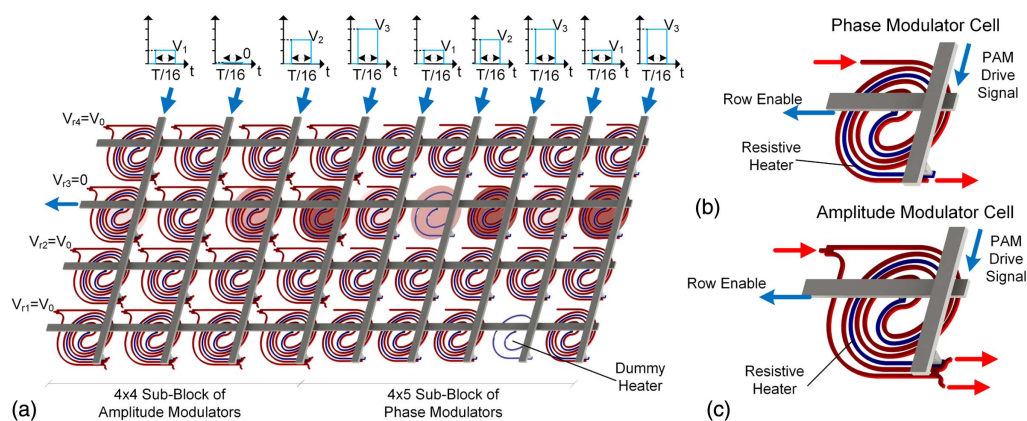
Fig. 5. Row–column drive scheme for amplitude and phase modulators. (a) Four out of 16 rows from the 16×9 row–column block. The elements in each row are programmed by forward-biasing the elements in that row while keeping all the other rows in reverse bias. Each row is active for $T/16$ of the programming cycle and programs all 16 elements in each row. (b) Implemented phase modulator using a compact spiral thermo-optic modulator. (c) Implemented amplitude modulator based on a tunable MZI splitter using a compact spiral modulator.
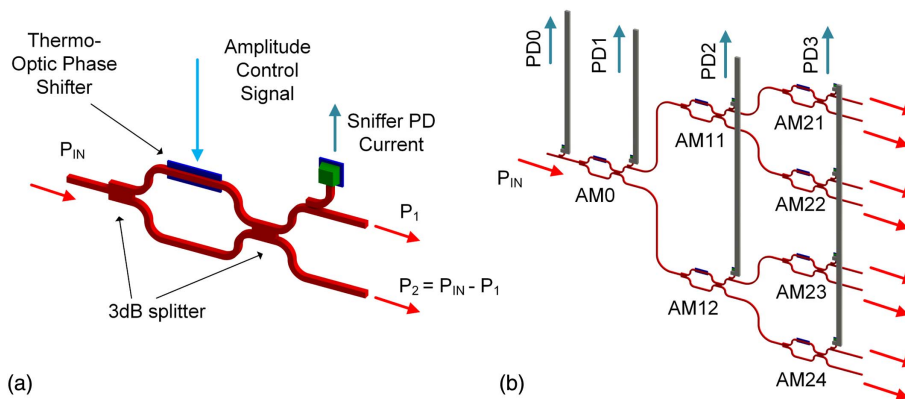
Fig. 6. Tunable amplitude modulation with calibration feedback. (a) Unit tunable power splitter with 1% sniffer output for control. (b) 1:8 tunable power splitter with reduced sensing interconnect complexity.

It can be noted that this calibration requires $2^N - 1$ sniffer diodes and $2^N - 1$ sensing nodes for a $1:2^N$ splitter array. However, since this calibration needs to be performed only once, it is possible to reduce the number of required sensing nodes to $N + 1$ by combining the output current of detectors in each stage and using a sequential calibration methodology. This methodology is described using the 1:8 splitter in Fig. 6(b). The output of the first sensing stage (PD1) can be used to calibrate the tunable coupler (AM0) in the first splitting stage. Afterward, AM0 is configured so that all power is delivered to AM11. As a result, the combined output of the second sensing stage (PD2) corresponds only to the top branch (AM11). This sensing output can be used to calibrate AM11. Iterating this process for all the remaining amplitude modulators allows full calibration of this 1:8 splitter using only four sensing nodes. For the 255-element array, only nine sensing nodes are required, which significantly reduces the sensing interconnect complexity.

In this OPA system implementation, the power is coupled into the aperture using a lensed grating coupler. An integrated PIN modulator isolates the coupled light from the scattered reflected light from the substrate. Integrated proportional-to-absolute temperature (PTAT) sensors can be used to measure the substrate temperature gradient across the chip. The optical path-length mismatch between radiating elements is compensated for by incorporating additional delay lines in the chip. The entire system has a 2.2 mm × 2.2 mm area.

4. MEASUREMENT RESULT

The amplitude and phase modulator unit cell with the compact spiral phase shifters was characterized in Ref. [29]. These modulators have a 19 kHz electro-optical bandwidth and require 21.2 mW for a 2π phase shift for the complete beamforming capability as well as the ability to correct for fabrication mismatches. The low 3 dB thermo-optical bandwidth (<100 kHz) of these thermal modulators is consistent with other such modulators reported in literature [30,31]. The power requirement for complete 2π control of the phase shifters means that the worst-case power consumption of these optical modulators will be 8.1 W. Therefore, thermal phase shifters are a potential

bottleneck in the scalability of OPAs. For the beamforming optimization of the annular-ring-aperture OPA, 36 PAM drivers with 10 bits of resolution and 64 row-enable switches with a 10 V maximum swing and 10 ns rise and fall time were used. The row–column drive circuits operate at a 1.56 MHz repetition rate, which is sufficiently larger than the thermal time-constant of the spiral modulators. Since all metal traces were designed based on the maximum expected current densities, no degradation in performances or failures in the interconnects or active devices were observed during the measurements.

The far-field radiation pattern of the OPA was captured using a custom optical far-field radiation measurement setup. This apparatus moves a compact InGaAs photodetector along the arc at a fixed distance with respect to the OPA chip and captures the far-field pattern point by point. The 1.55 μm light coupled into the chip is modulated at 1.1 MHz by the integrated on-chip PIN modulator. Therefore, the modulated optical power radiated from the aperture can be distinguished from the scattered light at the input grating coupler (due to fiber-to-chip coupling inefficiencies). Note that the on-chip PIN modulation frequency can be set to any value as long as it is within the electrical bandwidth limitations of the far-field measurement setup. This transmitter path modulation is compatible with time-domain encoding schemes such as FMCW and receiver architectures such as heterodyne receivers [6]. Furthermore, no interference between this transmitter path modulation and the drivers and phase shifters in the row–column drive scheme was observed during far-field beam optimization and characterization measurements. The far-field radiation power was filtered and quantized using a spectrum analyzer with 10 Hz resolution bandwidth. The collected power was normalized with respect to the power coupled into the chip to remove any changes in power due to the slight variations in the position of the input fiber during the measurement.

All of the phase and amplitude modulators in the array were optimized concurrently using the 36 PAM drivers. These PAM drivers switch between 16 different values with 10-bit resolution for the 16 different rows. During each iteration of beam optimization, the algorithm must optimize all the phase and amplitude modulators in each of the four 16 × 9 blocks.
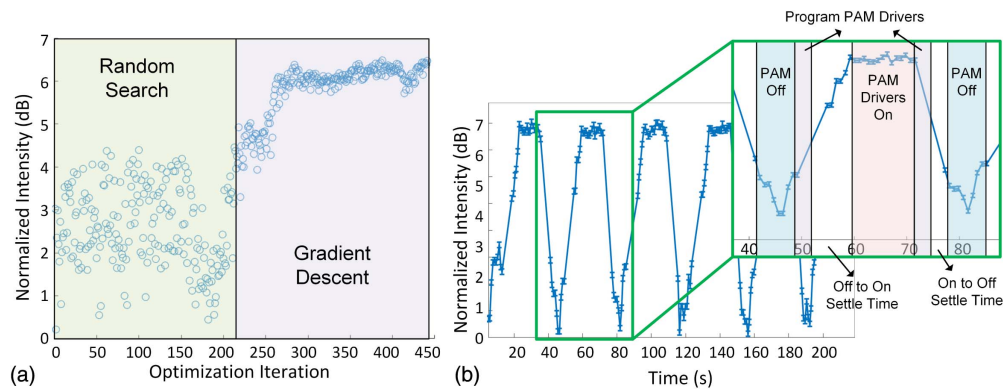
Fig. 7. (a) Beam power optimization progression after 450 iterations. (b) Dynamic stability and repeatability of the annular-ring OPA. The PAM drivers can maintain the optimized setting with less than 0.4 dB variations.

The large number of driver settings (576 drivers with 10-bit resolution) creates a large search space to find the optimized beam. Furthermore, due to fabrication mismatches, the initial phase setting of the aperture is random. Therefore, the beam pattern $P(\theta, \phi, \theta_0, \phi_0)$ and the required phase shift values for beam optimization $\phi_{n,m}$, as shown in Eq. (3), result in a non-convex search space that creates a challenge to find optimum beam patterns. To address this problem, we first performed a randomized optimization and recorded the broadside beam power value. During each optimization step, a new random set of 576 values is programmed in the phase and amplitude modulators, and the main beam power is measured. After 200 iterations, the randomized search found a PAM setting with 3–4 dB increased signal power in the main beam. Afterward, a modified gradient search continues to optimize the main beam power from the best randomly-optimized beam. In this step, the gradient search gradually increases or decreases each of the 576 programmed values to optimize the main beam power. After 250 iterations, the gradient descent improves the beam by approximately 2 dB. The optimization progression is shown in Fig. 7(a).

To verify the dynamic beamforming stability and repeatability of this OPA, we switched between the setting with all PAM drivers off and the optimum PAM setting for the broadside and

recorded the dynamic changes in the normalized main beam power (with respect to the power coupled into the chip) as a function of time. The dynamic stability of the PAM drive is shown in Fig. 7(b). It takes 2 s to program the 576 values into the 32 PAM drivers. The thermal gradient variations on the chip settle in approximately 8 s, which is the limiting factor for the total optimization time per beam direction. This thermal settling time is a function of the particular measurement setup and can be reduced by improving the substrate heat sink. The PAM drivers are able to consistently program the phase and amplitude modulators through the row–column drive scheme with less than 0.4 dB ripple in the peak power.

Afterward, we measured the optimized beam pattern using the aforementioned optical far-field measurement setup. The InGaAs photodetector was rotated along the arc in (θ_x, θ_y) directions at a 5 cm distance. A 2D scan of the optimized beam pattern for the broadside direction $(\theta_x, \theta_y) = (0°, 0°)$ in Fig. 8(a) shows no grating lobes in the measurement FOV of $(10°, 10°)$ limited by the measurement setup. This measurement was repeated three times and the cross-sectional views of the normalized broadside beam pattern with standard deviation for $\theta_y = 0°$ and $\theta_x = 0°$ are shown in Figs. 8(b) and 8(c), respectively. Due to fabrication mismatches, which create a random initial state for the phase shifter, the thermal
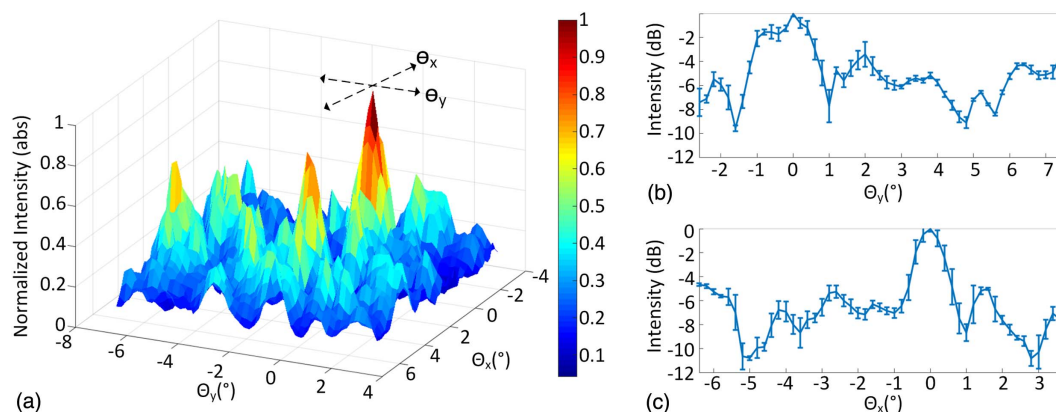
Fig. 8. 2D beamforming demonstration. (a) 2D beam pattern was measured for the optimized direction (0°, 0°). (b) 1D cross-sections of the beam pattern in θ_x ($\phi = 0°$ plane). (c) 1D cross-sections of the beam pattern in θ_y ($\phi = 90°$ plane).
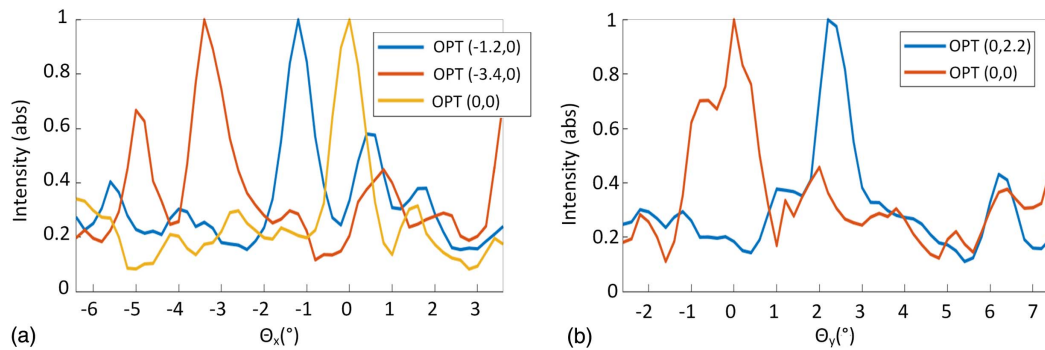
Fig. 9. Cross-sectional view of the beam pattern for several directions. (a) Phase-shifter-enabled beam steering in θ_x ($\phi = 0°$ plane) for two additional directions. (b) Phase-shifter-enabled beam steering in θ_y ($\phi = 90°$ plane) for an additional direction.

Table 1. Comparison of Recent 2D Aperture OPAs

	This Work	Caltech 2019 [29]	Caltech 2018 [6]	USC 2015 [27]	UPenn 2019 [7]	KIAST 2019 [2]	NUAA 2018 [21]
Aperture Type	Uniform polar	Sparse Cartesian	Uniform Cartesian	Uniform Cartesian	Uniform Cartesian	Uniform Cartesian, MEMS	Nonuniform polar
Number of Radiators (N)	255	128	8 × 8	8 × 8	8 × 8	160 × 160	73
Beamwidth	1°^{a}	0.8°	0.75°	0.45°	N/A^b	0.04° × 0.03°	N/A
SLL	–4 dB^a	–12 dB	–10 dB	–11 dB	N/A	–11/–18 dB	–11 dB^c
Steering Range	23° × 16.3°	16°	8°	1.6°	7°	6.6° × 4.4°	30°
Number of Maximum Resolvable Spots (S)	9315^c	400	113	12	N/A	25,600	N/A
Number of Drivers	100	32	64	129	16	N/A	N/A

^{a}Simulated beamwidth and SLL are 0.2° and –15.6 dB, respectively.
^{b}N/A: data not reported in the corresponding publication.
^{c}Based on simulation result.

crosstalk between modulators, and the large search space, the optimization method fails to reduce the SLL to the expected values from simulation. Nevertheless, the optimization method used here was able to reduce the SLL for the beam in the broadside direction $(\theta_x, \theta_y) = (0°, 0°)$ to –4 dB, which is sufficient to demonstrate beamforming. Finally, we demonstrated the beam-steering capability of this annular-ring aperture by optimizing the beam in several other directions. This was done by re-optimizing all the phase and amplitude modulators in the array using the aforementioned beam optimization methodology. The InGaAs detector was positioned at $(\theta_x, \theta_y) = (-1.2°, 0°)$ and $(\theta_x, \theta_y) = (-3.4°, 0°)$ to demonstrate beam steering in θ_x direction. It was also positioned at $(\theta_x, \theta_y) = (0°, 2.2°)$ to demonstrate beam steering in θ_y direction. The cross-sectional views of these steered beams are shown in Fig. 9.

5. CONCLUSION

In this work, we analyzed the advantages and design trade-offs of fixed linear density multi-annular-ring-aperture OPAs. Such OPAs reduce the sparse array design complexity due to their symmetric nature and permit signal distribution in a planar photonics process. Furthermore, the linear density of the elements in the OPA maintains a constant power efficiency for larger apertures, reducing the beamwidth and the SLL. In a standard photonics process, we implemented an annular-ring

aperture with 255 radiating elements and 510 phase and amplitude modulators. The performance of the proposed 2D aperture multi-annular-ring OPA is compared to other recent 2D aperture OPAs in Table 1. The proposed design uses a row–column drive, which reduces the electrical interconnect complexity from N^2 to $2N$. Furthermore, we measured the row–column drive programming reliability to be better than 0.4 dB. Finally, we measured the far-field radiation pattern of the aperture for several directions, demonstrating the beamforming and beam-steering capability for this aperture.

Disclosures. The authors disclose no conflicts of interest.

Data Availability. Data underlying the results presented in this paper are not publicly available at this time but may be obtained from the authors upon reasonable request.

REFERENCES

1. A. Tuantranont, V. Bright, J. Zhang, W. Zhang, J. Neff, and Y. Lee, "Optical beam steering using MEMS-controllable microlens array," Sens. Actuators A Phys. **91**, 363–372 (2001).

2. Y. Wang, G. Zhou, X. Zhang, K. Kwon, P.-A. Blanche, N. Triesault, K. S. Yu, and M. C. Wu, "2D broadband beamsteering with large-scale MEMS optical phased array," Optica **6**, 557–562 (2019).
3. F. Aflatouni, B. Abiri, A. Rekhi, and A. Hajimiri, "Nanophotonic coherent imager," Opt. Express **23**, 5117–5125 (2015).
4. S. Chung, M. Nakai, S. Idres, Y. Ni, and H. Hashemi, "Optical phased-array FMCW lidar with on-chip calibration," in *IEEE International Solid-State Circuits Conference (ISSCC)* (2021), Vol. **64**, pp. 286–288.
5. F. Aflatouni, B. Abiri, A. Rekhi, and A. Hajimiri, "Nanophotonic projection system," Opt. Express **23**, 21012–21022 (2015).
6. R. Fatemi, B. Abiri, and A. Hajimiri, "An 8 × 8 heterodyne lens-less OPA camera," in *Conference on Lasers and Electro-Optics* (2017), paper JW2A.9.
7. F. Ashtiani and F. Aflatouni, "N × N optical phased array with 2N phase shifters," Opt. Express **27**, 27183–27190 (2019).
8. M. S. Eggleston, F. Pardo, C. Bolle, B. Farah, N. Fontaine, H. Safar, M. Cappuzzo, C. Pollock, D. J. Bishop, and M. P. Earnshaw, "90 dB sensitivity in a chip-scale swept-source optical coherence tomography system," in *Conference on Lasers and Electro-Optics* (2018), paper JTh5C.8.
9. A. White, P. Khial, F. Salehi, B. Hassibi, and A. Hajimiri, "A silicon photonics computational lensless active-flat-optics imaging system," Sci. Rep. **10**, 1689 (2020).
10. C. V. Poulton, M. J. Byrd, P. Russo, E. Timurdogan, M. Khandaker, D. Vermeulen, and M. R. Watts, "Long-range LiDAR and free-space data communication with high-performance optical phased arrays," IEEE J. Sel. Top. Quantum Electron. **25**, 7700108 (2019).
11. S. A. Miller, C. T. Phare, Y.-C. Chang, X. Ji, O. A. J. Gordillo, A. Mohanty, S. P. Roberts, M. C. Shin, B. Stern, M. Zadka, and M. Lipson, "512-element actively steered silicon phased array for low-power LIDAR," in *Conference on Lasers and Electro-Optics* (2018), paper JTh5C.2.
12. J. Sun, E. Timurdogan, A. Yaacobi, E. S. Hosseini, and M. R. Watts, "Large-scale nanophotonic phased array," Nature **493**, 195–199 (2013).
13. S. Chung, H. Abediasl, and H. Hashemi, "A 1024-element scalable optical phased array in 0.18 μm SOI CMOS," in *IEEE International Solid-State Circuits Conference (ISSCC)* (2017), pp. 262–263.
14. N. Dostart, B. Zhang, A. Khilo, M. Brand, K. A. Qubaisi, D. Onural, D. Feldkhun, K. H. Wagner, and M. A. Popović, "Serpentine optical phased arrays for scalable integrated photonic lidar beam steering," Optica **7**, 726–733 (2020).
15. C. V. Poulton, M. J. Byrd, M. Raval, Z. Su, N. Li, E. Timurdogan, D. Coolbaugh, D. Vermeulen, and M. R. Watts, "Large-scale silicon nitride nanophotonic phased arrays at infrared and visible wavelengths," Opt. Lett. **42**, 21–24 (2017).
16. W. Ma, S. Tan, K. Wang, W. Guo, Y. Liu, L. Liao, L. Zhou, J. Zhou, X. Li, L. Liang, and W. Li, "Practical two-dimensional beam steering

system using an integrated tunable laser and an optical phased array," Appl. Opt. **59**, 9985–9994 (2020).
17. D. O'Neill, "Element placement in thinned arrays using genetic algorithms," in *Proceedings of OCEANS* (1994), Vol. **2**, pp. II/301–II/306.
18. R. Haupt, "Thinned arrays using genetic algorithms," IEEE Trans. Antennas Propag. **42**, 993–999 (1994).
19. C. Balanis, *Antenna Theory: Analysis and Design* (Wiley, 2015).
20. M. E. Bialkowski and N. C. Karmakar, "A two-ring circular phased-array antenna for mobile satellite communications," IEEE Antennas Propag. Mag. **41**, 14–23 (1999).
21. F. Zhang, D. Zhang, and S. Pan, "Fast and wide-range optical beam steering with ultralow side lobes by applying an optimized multi-circular optical phased array," Appl. Opt. **57**, 4977–4984 (2018).
22. N. H. Noordin, V. Zuniga, A. O. El-Rayis, N. Haridas, A. T. Erdogan, and T. Arslan, "Uniform circular arrays for phased array antenna," in *Loughborough Antennas Propagation Conference* (2011), pp. 1–4.
23. M. M. Khodier and M. Al-Aqeel, "Linear and circular array optimization: a study using particle swarm intelligence," Prog. Electromagn. Res. **15**, 347–373 (2009).
24. A. Austeng and S. Holm, "Sparse 2-D arrays for 3-D phased array imaging-design methods," IEEE Trans. Ultrason. Ferroelectr. Freq. Control **49**, 1073–1086 (2002).
25. A. Darbinian, S. A. Hajimiri, A. Khachaturian, and S. M. Fatemi, "Photonics adaptive beam forming with a polar lattice comprising optical phased array receiving elements to receive the steered optical beam from optical phased array transmitting elements positioned in a circular path," U.S. patent 11,245,471 (2022).
26. P. Ioannides and C. Balanis, "Uniform circular arrays for smart antennas," IEEE Antennas Propag. Mag. **47**, 192–206 (2005).
27. H. Abediasl and H. Hashemi, "Monolithic optical phased-array transceiver in a standard SOI CMOS process," Opt. Express **23**, 6509–6519 (2015).
28. J. K. S. Poon and W. D. Sacher, "Multilayer silicon nitride-on-silicon photonic platforms for three-dimensional integrated photonic devices and circuits," in *75th Annual Device Research Conference (DRC)* (2017), pp. 1–2.
29. R. Fatemi, A. Khachaturian, and A. Hajimiri, "A nonuniform sparse 2-D large-FOV optical phased array with a low-power PWM drive," IEEE J. Solid-State Circuits **54**, 1200–1215 (2019).
30. M. Jacques, A. Samani, E. El-Fiky, D. Patel, Z. Xing, and D. V. Plant, "Optimization of thermo-optic phase-shifter design and mitigation of thermal crosstalk on the SOI platform," Opt. Express **27**, 10456–10471 (2019).
31. N. C. Harris, Y. Ma, J. Mower, T. Baehr-Jones, D. Englund, M. Hochberg, and C. Galland, "Efficient, compact and low loss thermo-optic phase shifter in silicon," Opt. Express **22**, 10487–10493 (2014).